Instantaneous structure and statistical feature of unsteady flow in a channel obstructed by a square rod

Kenjiro Suzuki
Department of Mechanical Engineering, Kyoto University, Kyoto, Japan

Hiroshi Suzuki
Department of Mechanical Engineering, Hiroshima University, Higashi-Hiroshima, Japan

A two-dimensional numerical computation has been made for an unsteady flow in a channel obstructed by an inserted square rod. The results of the computation made for the flow with a parabolic inlet velocity profile at a specific value of channel Reynolds number are analyzed in detail. The obtained results reveal that momentum transfer is enhanced due to the apparent shear stress resulting from the nonzero value of cross-correlation between the streamwise and normal components of fluctuating velocity, $\overline{uv}$, just as in turbulent shear flows, although the studied flow is quite different from turbulent flows in the sense that it is highly periodical and therefore free from randomness. This periodicity leads to a quick recovery of the velocity defect in some region of the wake of the rod. Special attention is paid to the time variation of flow structure. The crisscross motion of the Karman vortex previously found to occur is discussed again, and how it appears is explained in terms of the interaction between the Karman vortex and the disturbed wall shear layer. In the discussion of this relationship, wavering motion of the separation vorticity layers formed on both sides of the rod and the periodic formation of an isolated vortex island from the lifted tip of the wall vorticity layer are analyzed. The vortex island is found to play an important role not only for the occurrence of the crisscross motion of Karman vortex but also for the generation of the nonzero value of $\overline{uv}$.

Keywords: unsteady channel flow; numerical analysis; obstruction with a square rod; cross-correlation; wall vortex; quadrant analysis

Introduction

It is well known that heat transfer can be enhanced under a periodically changing unsteady laminar flow. In recent years, such an unsteady flow has been attracting much attention (Nishihara et al. 1988; Xi et al. 1989; Kikuchi et al. 1993; Lehmann and Wirtz 1988; Karniadakis et al. 1988; Davis et al. 1984; Davis and Moore 1982; Majumder and Amon 1992; Tatsutani et al. 1993). However, the instantaneous structure of the flow has not been studied sufficiently, mainly due to the difficulty of the experimental measurements. In an earlier study (Suzuki et al. 1993), a numerical computation related to some practical applications was made for the unsteady flow formed downstream of a square rod mounted in a channel. A crisscross motion of the Karman vortex was found to occur when the ratio of the rod size to the channel height was not too small, and some detailed examination was made of the conditions under which such motion appears. The presence of a wall was suggested to be very important in the generation of such vortex motion, but its effect was not analyzed in detail. The present article deals with the same type of unsteady flow and attempts to clarify how this crisscross motion of the vortex appears. The instantaneous structure of the flow is analyzed from this perspective. Additionally, the statistical features of this flow are studied in detail. Particular attention is paid to the nonzero value of $\overline{uv}$, the cross-correlation between the streamwise and normal components of velocity fluctuation, which makes the velocity defect in the wake of the inserted rod recover at a faster rate at some streamwise positions. This nonzero value of $\overline{uv}$ is also discussed in terms of the instantaneous behavior of the flow. Detailed analysis of the flow structure reveals that fluid motions such as the wallward and outward interactions of near-wall turbulence are intensified in the downstream region of the rod. Those fluid motions were previously reported to cause the dissimilarity between the heat and momentum transfer in a turbulent boundary layer disturbed by a cylinder (Kawaguchi et al. 1984; Suzuki et al. 1988; Suzuki et al. 1991). Such dissimilarity was actually found previously for the present type of unsteady flow (Suzuki and Suzuki 1994). The analysis of this type of unsteady flow may also suggest how unsteady turbulent flow observed behind a bluff body (Frank and Rodi 1991; Deng et al. 1993; Kato and Launder 1993) should be modeled.

Address reprint requests to Professor H. Suzuki at the Department of Mechanical Engineering, Hiroshima University, Higashi-Hiroshima 724, Japan.

Received 9 January 1993; accepted 22 June 1994

Numerical models and procedures

The finite-difference equivalents of two-dimensional (2-D), time-dependent momentum equations were numerically solved. The numerical models and procedures adopted in the present

computation are the same as those used previously (see Suzuki et al. 1993), so they will be outlined here very briefly. The momentum equations are written as follows:

$$\frac{\partial}{\partial t}(\rho U)+\frac{\partial}{\partial x}(\rho U^2)+\frac{\partial}{\partial y}(\rho VU)=-\frac{\partial P}{\partial x}+\frac{\partial}{\partial x}\left(\mu\frac{\partial U}{\partial x}\right)+\frac{\partial}{\partial y}\left(\mu\frac{\partial U}{\partial y}\right) \quad (1)$$

$$\frac{\partial}{\partial t}(\rho V)+\frac{\partial}{\partial x}(\rho UV)+\frac{\partial}{\partial y}(\rho V^2)=-\frac{\partial P}{\partial y}+\frac{\partial}{\partial x}\left(\mu\frac{\partial V}{\partial x}\right)+\frac{\partial}{\partial y}\left(\mu\frac{\partial V}{\partial y}\right) \quad (2)$$

Constant properties were assumed for the working fluid. A third-order upwind model (QUICK (Leonard 1979)) was applied for finite differencing of the convection terms, and central finite differencing was used for the diffusion terms. Fully implicit forms of the finite-difference equations thus obtained were solved successively along the time axis step by step. An iterative procedure was adopted in the calculation at each time step to correct the solution for the pressure field so as to match the updated velocity field better. The pressure field was calculated by following the SIMPLE algorithms (Patankar and Spaulding 1972).

Grid points totaling 207 × 54 were allocated nonuniformly in the computational domain (Figure 1) finely close to the edges of the rod. The streamwise length of the domain was set equal to 12 times the channel height, or $12H$, and a square rod was located at a position $2H$ downstream from the upstream end of the computational domain. x and y designate the streamwise and normal coordinates, respectively, and the origin of the coordinate system was located at the center of the rod. Suzuki et al. (1993) discuss the numerical results for various cases using different rod sizes, different inlet flow conditions, and different Reynolds numbers. The present analysis focuses mainly on one typical case of the rod size, $d/H = 0.3$, but in a very detailed manner. At the upstream boundary, the inlet flow was assumed to be steady, laminar, and hydrodynamically fully developed, i.e., having a parabolic velocity profile. The channel Reynolds number, Re, based on the hydraulic equivalent diameter of the channel, $2H$, and on the cross-sectional average velocity, U_m, was kept at 1,000.

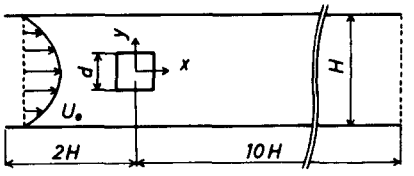

Figure 1 Computational domain

A no-slip condition was applied as the boundary condition along the solid wall. The boundary condition at the downstream end of the computational domain was given based on the assumption that the flow field there should obey the boundary-layer approximation (Suzuki 1981). The computation began with an imaginary flow field as the initial condition, and an analysis was made of the computed flow field obtained at the stage about 20 cycles after the shedding frequency of Karman vortex reached an asymptotic value. The computed results obtained at this stage were previously confirmed to be independent from the initial conditions.

Apparatus and procedures for the heat transfer experiment

Figure 2 is a schematic of the experimental apparatus used for the simultaneous measurements of streamwise and normal velocity components, u and v. Air was sucked into a duct by a blower, and the flow rate was measured at the end of the system. The height of the duct, H, is 50 mm, and the duct aspect ratio was eight. The duct length before the entry to the test section was about 4,500 mm, corresponding to almost 90 times the duct height. Therefore, hydrodynamically fully developed flow was established at the inlet to the test section. This was confirmed experimentally by measuring the velocity profile in the channel with a hot-wire anemometer.

Notation

C_P	Pressure coefficient ($=2(P-P_0)/\rho U_m^2$)
c_P	Fluctuating pressure coefficient ($=2(P-\bar{P})/\rho U_m^2$)
d	Size of square rod (m)
dV_{Pi}	Contribution to V_P from the regions specified in Figure 17
E	Output of hot-wire anemometer (V)
H	Distance between two parallel flat plates (m)
H'	Hole size used in quadrant analysis
I_i	Indicator used in quadrant analysis
P	Pressure (Pa)
Re	Channel Reynolds number ($=2\rho U_m H/\mu$)
Re_d	Rod Reynolds number ($=\rho U_m d/\mu$)
t	Time (s)
U	Streamwise velocity (m/s)
u	Fluctuating streamwise velocity (m/s)
$\widetilde{uv}_i$	Contribution to $\overline{uv}$ from the ith quadrant of the u–v plane (m^2/s^2)
V	Normal velocity (m/s)
V_d	Normal velocity induced by distributed vorticity elements (m/s)
v	Fluctuating normal velocity (m/s)
x	Streamwise coordinate (m)
y	Normal coordinate (m)

Greek symbols

η	Streamwise distance (m)
θ	Angle between y-direction and induced velocity vector (rad)
μ	Viscosity of fluid (Pa·s)
ξ	Normal distance (m)
ρ	Density of fluid (kg/m^3)
τ	Shear stress (Pa)
Ω	Vorticity (s^{-1})
ω	Angular frequency (rad/s)

Subscripts

m	Cross-sectional mean
P	Center of Karman vortex
w	Wall
0	Inlet

Superscripts

′	Intensity
-	Time mean

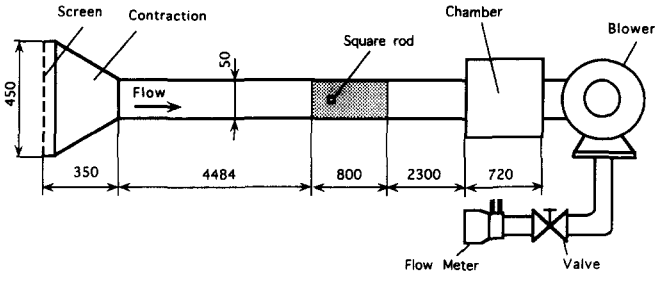

Figure 2 Experimental apparatus

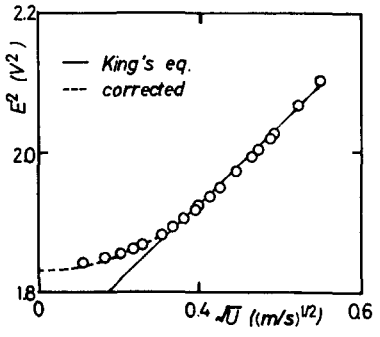

Figure 3 Static characteristics of hot-wire anemometry

Simultaneous measurements of streamwise and normal components of velocity fluctuations were carried out with an X-type hot-wire probe for the case of $d/H = 0.3$ and Re = 1,000. Prior to the experiments, static calibration was made for each wire of the probe, positioning it in the center plane of the duct at a streamwise position where the fully developed steady laminar flow was confirmed to be established over the whole velocity range. In the very-low-flow velocity region, the squared value of the hot-wire signal plotted against the root value of flow velocity (Perry 1982) becomes nonlinear, as shown in Figure 3. The calibration data were approximated by a quadratic equation in this velocity range (Suzuki 1990). The measurements were performed at four streamwise locations, namely, $x/H = 1.5$, 2.0, 3.0, and 4.0, where no adverse flow was confirmed to exist. Each of the output signals from the two anemometers was digitized on line at the sampling rate of 400 Hz and recorded on a magnetic tape. Linearization and processing of the data were later done by a computer at the Kyoto University Data Processing Center.

Results and discussion

In the following discussion, how the time-averaged flow field develops downstream will first be described. Figure 4 shows the streamwise distribution of the nondimensional form of time-mean pressure. The solid curve in the figure shows the value along the wall and the dotted curve shows the cross-sectional mean. The flow under study is not a boundary-layer type, so the pressure can be nonuniform in a cross section. Therefore, in the region between $x/H = -0.8$ and $x/H = 2.0$, the two curves do not coincide with each other. However, they show a similar recovery of pressure or increase of pressure towards the downstream in the region $0.5 < x/H < 2.0$. Upstream of $x/H = -1.0$ and downstream of $x/H = 2.0$, the two curves almost coincide with each other and indicate a linear streamwise distribution of pressure. In those regions, flow is expected to be close to the fully developed state. The vertical distance between the two lines, ΔC_P, corresponds to the form drag of the inserted rod, which is much larger than the pressure drop occurring due to the shear stress acting on the channel walls over the whole computational domain.

Figure 5 shows how the cross-sectional distributions of the time-averaged velocity components $\bar{U}$ and $\bar{V}$, the fluctuation intensities of streamwise and lateral components of velocity, u' and v', and the cross-correlation $\overline{uv}$ develop along the streamwise direction. In this figure, the solid lines and symbols indicate the data obtained numerically and experimentally, respectively.

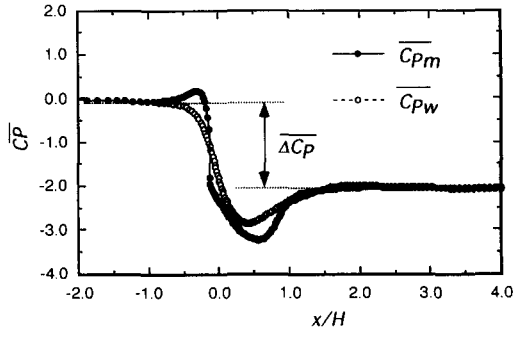

Figure 4 Streamwise distribution of time-averaged pressure coefficient

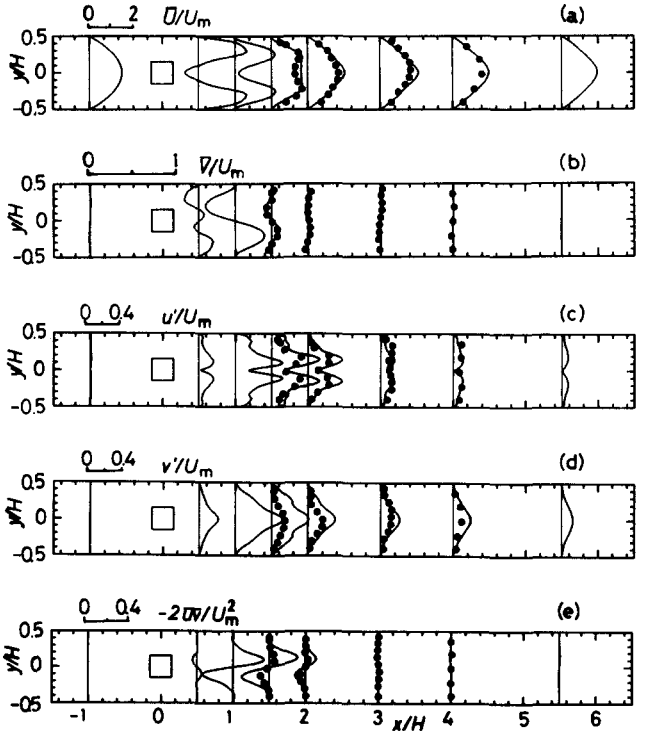

Figure 5 Streamwise variations of statistical values (—, numerical data; •, experimental data). (a) Cross-sectional distribution of time-averaged streamwise velocity; (b) cross-sectional distribution of time-averaged normal velocity; (c) cross-sectional distribution of intensity of streamwise fluctuating velocity; (d) cross-sectional distribution of intensity of normal fluctuating velocity; (e) cross-sectional distribution of cross-correlation between streamwise and normal components of fluctuating velocity

The effect of the inserted rod on the flow structure does not reach its upstream side in a noticeable fashion. Therefore, the $\bar{U}$-profile at the station $x/H = -1.0$ is still very close to the parabolic profile given at the inlet, as shown in Figure 5a. At $x/H = 0.5$, the station (5/3)d downstream from the center of the rod, the existence of a back flow is clearly observed in the central part of the wake. A velocity decrease existing in the wake causes the flow acceleration outside the wake. Therefore, the maximum velocity at this station is more than twice the cross-sectional mean of the time-averaged velocity U_m. Thus, the velocity gradient in the shear layer of the wake is much larger than that found at the same streamwise station of the wake of the rod placed in a uniform flow. The profile at $x/H = 1.0$ is rather close to that at $x/H = 0.5$, although back flow is not observed any longer at $x/H = 1.0$. However, recovery of the $\bar{U}$-profile proceeds rapidly for a short distance after $x/H = 1.0$. At the next station, $x/H = 1.5$, the profile is quite different from those at upstream positions. It is almost flat in its central part. The profile resembles that of a developing region of channel flow, and the velocity gradient is large only in the regions close to the channel walls. At the two stations $x/H = 1.0$ and $x/H = 1.5$, the velocity profile has an inflection point in the region near the wall at $0.3 < y/H < 0.4$. This is reasonable, because the time-averaged form of the momentum equation for the streamwise velocity $\bar{U}$ (Equation 1) on the channel wall takes the form

$$\frac{\partial}{\partial y}\left(\mu \frac{\partial \bar{U}}{\partial y}\right) = \frac{\partial \bar{P}}{\partial x} \qquad (>0) \tag{3}$$

where the time-mean pressure $\bar{P}$ increases downstream at these stations, as previously seen in Figure 4. However, the y-direction second derivative of $\bar{U}$ cannot be positive at all y-positions, and it should become negative at some y-positions. Thus, the existence of an inflection point for the $\bar{U}$ profile is quite normal. The recovery of the time-averaged velocity field still proceeds rather rapidly down to the next station. At $x/H = 2.0$, the profile takes a shape quite different from those at $x/H = 1.0$ and $x/H = 1.5$: it has a maximum at the center. However, the recovery of the velocity profile is very much slowed down after this station. Even at $x/H = 4.0$, the profile still resembles that at $x/H = 2.0$ and yet clearly differs from the parabolic profile to be attained finally at far-downstream positions. Thus, a large distance will be necessary even after $x/H = 4.0$ before the velocity profile recovers completely. Therefore, the recovery of velocity profile does not proceed smoothly. It proceeds rapidly in one region and slowly in another region.

The time-averaged value of the normal velocity $\bar{V}$ shown in Figure 5b is almost zero over an entire cross section at $x/H = -1.0$ because the distribution of $\bar{U}$ deviates little from the parabolic profile at this station. Back flow in the central part of the wake should be decelerated towards the upstream from $x/H = 0.5$ to the back surface of the rod ($x/H = 0.15$). Thus, the following inequality holds in the central part of the channel at $x/H = 0.5$:

$$\frac{\partial \bar{U}}{\partial x} < 0 \tag{4}$$

Therefore, the following equation is suggested to hold from the continuity equation for the central part of the channel at $x/H = 0.5$:

$$\frac{\partial \bar{V}}{\partial y} > 0 \tag{5}$$

Just outside the back flow region, on the other hand, recovery of the velocity defect proceeds downstream, aided by the supply of fluid from the near-wall region. This means that $\bar{V}$ should be negative near the top wall and positive near the bottom wall. Therefore, it is reasonable that the cross-sectional profile of $\bar{V}$ has three zero-crossing points at this streamwise station. At $x/H = 1.0$, there is already no back flow. Therefore, the $\bar{V}$ profile at this station has no such a central region as obeying Equation 4, and it resembles the counterpart for the wake of a rod placed in a uniform flow. At $x/H = 1.5$ and $x/H = 2.0$, flow acceleration occurs around the center plane and, in a less remarkable manner, near the wall. These accelerations take place due to the supply of fluid from the high-velocity region, i.e., midway between the center plane and channel wall. Therefore, the $\bar{V}$ profile again displays three zero-crossing points at these two streamwise stations. At stations further downstream, $\bar{V}$ shows a value of almost zero across the channel height because the streamwise development of the $\bar{U}$ profile is very much slowed down there.

In order to explain the rapid recovery of the velocity defect found in the near-wake region of the rod, the statistical quantities of the fluctuating velocity field will be discussed next. Figures 5c and 5d show the streamwise development of the cross-sectional distributions of the intensities, respectively, of the streamwise and cross-stream components of the fluctuating velocity, u' and v'. The cross-sectional profile of u' at each streamwise station has two maxima in the separation shear layers developing on both sides of the channel center plane, while that of v' has only one peak at the center of the channel. The peak value of u' increases steeply from $x/H = 0.5$ to $x/H = 1.0$, and it takes a value larger than 50 percent of the cross-sectional average velocity, U_m, at $x/H = 1.0$ and $x/H = 1.5$. The peak value of u', still large at $x/H = 2.0$, is about 0.4 U_m. However, it decreases after that station and becomes as low as 0.1 U_m by $x/H = 4.0$. The peak value of v' also steeply increases from $x/H = 0.5$ to $x/H = 1.0$. It reaches a value larger than 0.5 U_m at $x/H = 1.0$. At $x/H = 1.5$, the peak value remains at a level of about 0.4 U_m but then decreases rather rapidly, although a little more slowly than u'. At $x/H = 3.0$, it is about 0.3 U_m, and it becomes as low as 0.2 U_m at $x/H = 4.0$.

One of the interesting features of the present flow is found in Figure 5e, in which the spatial distribution of cross-correlation between the streamwise and normal components of fluctuating velocity, $\overline{uv}$, is plotted. Since the present unsteady flow is highly periodic, the irregularity of velocity fluctuation is very weak in both time and space (Suzuki et al. 1993). Therefore, it is totally different from turbulent flows that are characterized by irregularity of fluctuations of velocity and of any other variable quantities. However, the present flow is still akin to turbulent flows in the sense that the cross-correlation $\overline{uv}$ takes a nonzero value or that the mixing is enhanced by the velocity fluctuation. As seen in Figure 5e, the peak value of cross-correlation is large at the three stations $x/H = 1.0$, 1.5, and 2.0. Thus, the apparent shear stress $-\overline{uv}$ acts noticeably in such flow regions, and should cause additional momentum transfer other than that caused by viscous force. The wall shear stress for the flow having a parabolic velocity profile and the cross-sectional average velocity U_m is given as follows:

$$\tau_w = 6\mu \frac{U_m}{H} = \frac{12}{\mathrm{Re}} \rho U_m^2 \ [\mathrm{Pa}] \tag{6}$$

The largest value of the apparent shear stress found in Figure 5e is about 0.15 ρU_m^2, which is about 12 times larger than the value given by Equation 6. It is several times larger even in comparison with the maximum viscous shear stress corresponding to the largest velocity gradient found in Figure 5a. Therefore, the quick recovery of the time-averaged flow field as found in the streamwise region of $1.0 < x/H < 2.0$ is concluded to be caused by the action of the apparent shear stress due to velocity fluctuation. Incidentally, Figure 5e also

shows that the value of $\overline{uv}$ is almost zero in the layers of some thickness adjoining the channel walls. The layer looks much thicker, at least on the absolute scale, compared to the viscous sublayer of wall turbulent flows. The reason is that, in the present flow, fluctuation cannot penetrate so close to the wall as in the wall turbulent flows of higher Reynolds number. However, the thickness is about 10 in the wall unit evaluated with friction velocity, so the thickness is not very different from that of the viscous sublayer for wall turbulent flows in nondimensional scale.

In a comparison of the obtained numerical results with the plotted experimental data, it is found that the time-averaged streamwise velocities and the normal velocities agree well. On the other hand, agreement is not very good for u', v', and $\overline{uv}$, especially at $x/H = 1.5$, where an extremely high intensity of the fluctuating velocity is observed. Kawall et al. (1983) and Nagano and Tagawa (1988) analyzed the inaccuracy of the streamwise and lateral velocities in high-intensity turbulent flows simultaneously measured with X-type hot-wire anemometry. These studies suggest that the measured values of u', v', and $\overline{uv}$ are noticeably smaller than their actual values. The inaccuracy of the measured data becomes larger as the turbulent intensity u' of the flow becomes larger. The analysis of these authors indicates that the inaccuracy of the measured $\overline{uv}$ remains about 5 to 7 percent when $u'/\bar{U} = 0.2$ in a typical turbulent boundary layer, but it becomes as large as 12 to 18 percent when $u'/\bar{U} = 0.3$. In the present study, the computed peak value of $u'/\bar{U}$ becomes as large as 0.5 at $x/H = 1.5$, and the disagreement between experimental and numerical data is the most remarkable there. However, the difference between these data becomes smaller as the turbulent intensity u' decreases towards the downstream. Therefore, the inaccuracy of the hot-wire anemometry is considered to be a main cause of the discrepancy between the present numerical and experimental results. On the other hand, the present experimental data are found to agree well qualitatively with the numerical results, in the sense that each distribution is similar in shape to the corresponding numerical one. Very importantly, the experimental data of cross-correlation, $\overline{uv}$, are confirmed to take a nonzero value at $x/H = 1.5$. This finding suggests the validity of the present numerical results. A comparison of both results will be discussed again later.

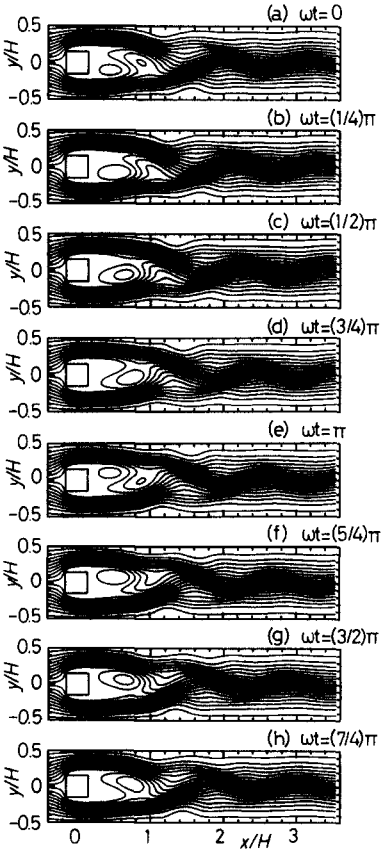

Figure 6 Time variation of instantaneous streamlines

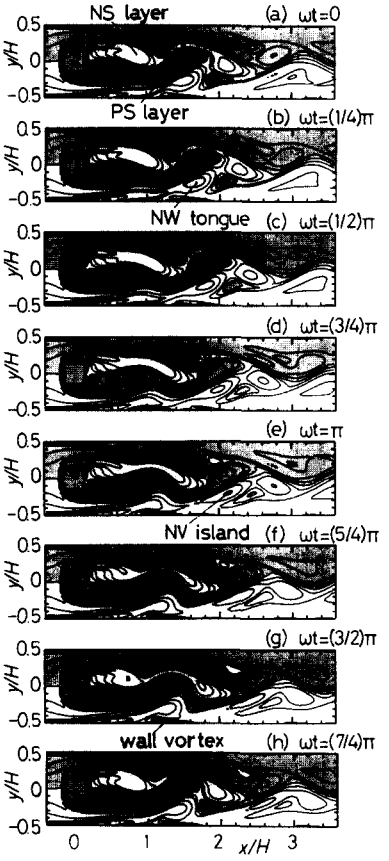

Figure 7 Time variation of instantaneous vorticity contours

In order to deepen the understanding of how the nonzero value of $\overline{uv}$ is generated in the present type of periodically changing unsteady flows, the time variation of the instantaneous flow structure will be discussed next. In this discussion, the crisscross motion of vortex found in Suzuki et al. (1993) will be discussed again in terms of the instantaneous flow structure, and some other related aspects of the flow structure will also be pointed out.

Figures 6 and 7 present the time sequence of instantaneous flow structure. Figure 6 shows the instantaneous streamlines and Figure 7 the instantaneous vorticity contours. The shaded parts of Figure 7 correspond to the regions where vorticity is positive in sign. Suzuki et al. (1993) clarified that the flow fluctuates in a highly periodic manner with a single frequency. Each frame in Figures 6 and 7 was sampled at every one-eighth of the period of the velocity fluctuation.

In the region $x/H < 0.3$, the flow is accelerated because of the flow obstruction caused by the inserted rod, but remains very steady in the region. The following discussion will focus on the flow structure in the region $x/H > 0.3$, where flow unsteadiness is clearly noticeable.

The first point of interest is the high-vorticity layers corresponding to the separation layers that develop from the two upstream corners of the rod. One of these, which is characterized by positive vorticity, is here called the Positive Vorticity Separation Layer (PS layer), and the other, which is characterized by negative vorticity, is called the Negative Vorticity Separation Layer (NS layer). As seen from the y- direction back-and-force motion of the interface between the PS and NS layers in Figure 7, a noticeable fluctuation of the cross-stream velocity component does exist at the position $x/H = 0.5$. As found in Figure 6, this is the streamwise position where the vortex to be periodically shed downstream starts to grow. Therefore, fluctuation of the streamwise velocity component is also expected to exist there. However, since the absolute value of velocity is not high at this point, the fluctuation of streamwise velocity cannot be very intense. At $x/H = 1.0$ and its downstream positions, both the PS and NS layers show a wavering motion while they move downstream. The motion is also accompanied by an elongation and therefore a thinning of the layers, so that the downstream tip of each layer is intermittently disconnected from its upstream main part. For instance, the downstream tip of the NS layer located around $x/H = 1.7$ in Figure 7d moves further downstream through several frames after Figure 7d. The neck of the NS layer, connecting its downstream tip and its main body attached to the rod surface, is then lifted upward. Therefore, a bending and thinning of the neck proceeds. After one time-period cycle is complete, a disconnection of the neck occurs as seen between Figures 7c and 7d. A similar time variation occurs in the PS layer with a half-cycle time lag. The disconnected tip of each layer is further separated into two parts of different sizes. This separation is completed between Figures 7e and 7f. Its smaller fraction remains in the region of positive vorticity, but disappears rather quickly. However, its larger fraction crosses the center plane of the channel, goes into the region of negative vorticity, and therefore reinforces the strength of vorticity field there. As is found in Figures 7h and 7a, this fraction moves further ahead, thrusts through the disconnected part of the PS layer, and separates it into two parts. This motion of the disconnected head of each vorticity layer and its succeeding motion, i.e., the crosscross motion of the center plane, correspond to the crisscross motion of the vortex reported by Suzuki et al. (1993).

The wavering motion of the PS or NS layer produces another important unsteady behavior of the flow. High-vorticity wall layers developing on the channel walls are intensified in vorticity beside the rod due to the flow acceleration occurring in the spaces between the rod and the channel walls. The tips of these high-vorticity wall layers are lifted at a certain streamwise position, as seen in all parts of Figure 7. Spatial distributions of time-averaged pressure and instantaneous fluctuating pressure sampled at every one-eighth period of flow fluctuation are respectively shown in Figure 8o and Figure 8a to 8h. Although the pressure field is perturbed by the formation and streamwise motion of local minima and maxima of pressure, as shown in Figures 8a to 8h, pressure along the channel wall increases at any instant towards the downstream at the streamwise positions of $0.4 < x/H < 0.6$. This adverse pressure gradient steadily causes the separation of wall high-vorticity layers in that streamwise region. The lifting of the wall high-vorticity layer, called the high-vorticity tongue or NW tongue below, in the case where vorticity is negative is followed by the elongation and thinning of the tongue proceeding in its root part. Thus, as found in Figure 7e, the tip of the high-vorticity tongue (NW tongue) is periodically cut off from the main part of the tongue and forms an isolated negative-vorticity island (NV island). In Figure 8g, the instantaneous value of the fluctuating pressure takes a

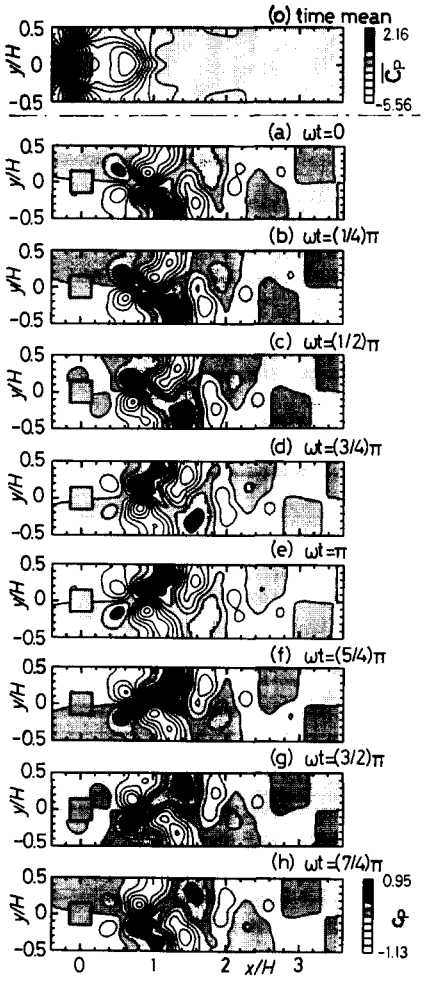

Figure 8 Pressure coefficient contours. (o) Time-averaged pressure contours; (a)–(h) time variation of instantaneous fluctuating pressure contours

minimum upstream of the tip of the PS layer. Thus, the adverse pressure gradient on the bottom wall is intensified there. This intensification of the adverse pressure gradient aids the separation of the NW tongue from the wall.

In connection with the formation of the high-vorticity tongue, another high-vorticity region of opposite sign appears in a thin region between the high-vorticity tongue and the wall. In Figure 7a, for instance, such a region extends from $x/H = 1.3$ to $x/H = 1.9$. In addition to this region, another developing region is observed at the position around $x/H = 0.8$. These thin high-vorticity regions adjoining the wall are called "wall vortexes" in the present article. The wall vortex develops due to the clockwise motion of fluid or the backward near-wall flow induced by the negative vorticity distributed in the NW tongue.

The nonzero value of the correlation $\overline{uv}$ described above will now be discussed from structural viewpoint. Figure 9 is a magnification of Figure 7 and shows the time variation of the instantaneous vorticity contours in the lower half of the channel space. Figure 10 shows the time traces of the streamwise and normal velocity components, u and v, and of their instantaneous products, uv, monitored over one period of flow fluctuation at the three points α, β, and γ, whose positions are indicated by the symbol " + " in Figure 9. The letters (a), (c), (e), and (g) on the top of Figure 10 indicate the instant at which the corresponding frames of Figures 6 through 9 are sampled. The values of the statistical quantities u' and v' used in the

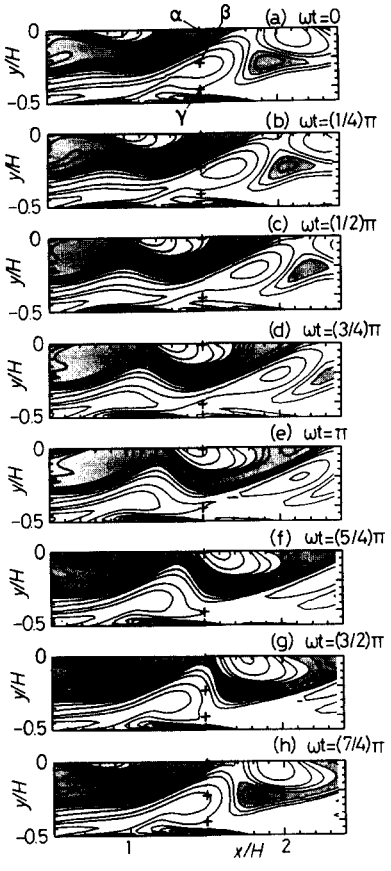

Figure 9 Time variation of instantaneous vorticity contours of the lower-half space in the channel

normalization of those three quantities at the three points are tabulated in Table 1 for reference, together with the value of $\overline{uv}$.

It is observed in Figure 10 that the fluctuating velocities, u and v, and the instantaneous products uv are changing with time. At the point α, the time-mean value of $\overline{uv}$ is small, as seen in Figure 5e or in Table 1. Thus, it is reasonable that the instantaneous value of uv fluctuates around zero. However, this is not the case for point β. At this point, uv takes a positive value for most of the time of one period of flow fluctuation. This results in a nonzero value of the time mean value $\overline{uv}$, as observed in Figure 5e. In particular, a sharp negative peak for $-uv$ occurs near the instant when positive peaks of u and v occur. This instant corresponds to the time when the interface between the thin neck of the PS layer and NW tongue that has been lifted from the wall passes the point β, as observed in Figure 9. On the other hand, another negative peak of $-uv$ appears around the instant when the negative peak for v occurs, a little after the appearance of the negative peak of u. This is the instant when the front of the NW tongue reaches the point β. Thus, the wavering motion of the PS layer and the accompanying motion of the NW tongue is the flow structure that causes the nonzero value of $\overline{uv}$ in the present unsteady flow.

Figure 11 shows Lissajous's figures for the fluctuating velocity components u and v obtained at the three positions α, β, and γ. Each curve, rather than being drawn by line, is composed of the series of the points sampled at a regular time interval. This method of presentation makes it possible to see how large a time fraction is spent in each quadrant of the u–v plane. Figures 12 and 13 show the fractional contribution from each quadrant of u–v plane to the cross-correlation $\overline{uv}$. Each quadrant of the u–v plane was named following the normally adopted method for the study of flow structure in a turbulent boundary layer (Kawaguchi et al. 1984; Suzuki et al. 1988; Suzuki et al. 1991; Lu and Willmarth 1973):

1st quadrant ($u > 0$ and $u > 0$); outward interaction

2nd quadrant ($u < 0$ and $v > 0$); ejectionlike motion

3rd quadrant ($u < 0$ and $v < 0$); wallward interaction

4th quadrant ($u > 0$ and $v < 0$); sweeplike motion

These names of fluid motions will be used in the present study for the motions observed in the lower half of the channel. The fractional contribution for each type of fluid motion classified above was calculated as follows:

$$\widetilde{uv}_i(H') = \lim_{T\to\infty} \frac{1}{T}\int_0^T uv(t) I_i(t, H')dt \quad (i = 1, 2, 3, 4) \tag{7}$$

$$I_i(t, H') = \begin{cases} 1 & \text{if } |uv(t)| > H'u'v' \\ & \text{and the point } (u, v) \text{ in the } u\text{–}v \text{ plane} \\ & \text{is in the } i\text{th quadrant} \\ 0 & \text{otherwise} \end{cases}$$

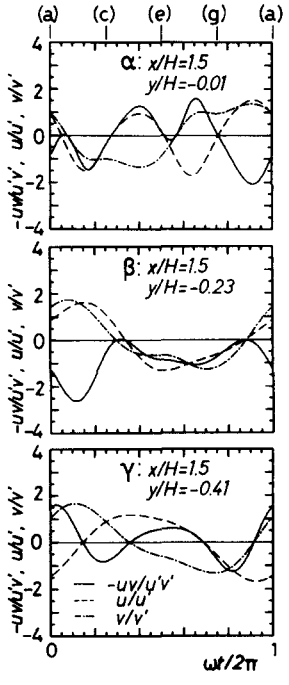

Figure 10 Time trace of streamwise and normal velocities and of the product $-\overline{uv}$

Table 1 Statistical values at points α, β, and γ

	x/H	y/H	U/U_m	u'/U_m	v'/U_m	$-2\overline{uv}/U_m^2$	$\overline{uv}/u'v'$
α	1.5	−0.01	1.37	1.58×10^{-1}	4.23×10^{-1}	-1.88×10^{-2}	0.141
β	1.5	−0.23	1.26×10^{-1}	2.99×10^{-1}	2.42×10^{-1}	-1.31×10^{-1}	0.905
γ	1.5	−0.41	3.34×10^{-1}	1.50×10^{-1}	7.88×10^{-2}	1.84×10^{-3}	−0.0778

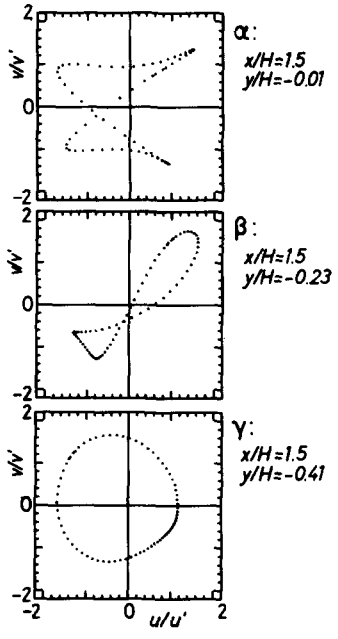

Figure 11 Lissajous's figures on the u–v plane

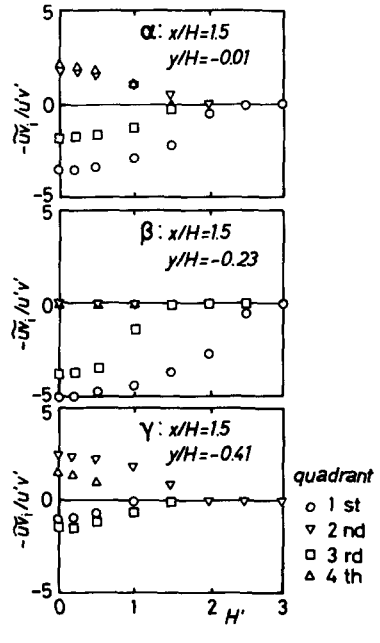

Figure 12 Fractional contibutions from the ith quadrant to $\overline{uv}$

Figure 12 plots the results obtained at the three points α, β, and γ against the hole size parameter H', which was introduced to distinguish the intensive fluid motion (characterized by the large value of the $u \times v$ product) from the less intensive ones. Figure 13 shows the cross-stream distribution of the fractional contribution to $\overline{uv}$ from the ith quadrant for the lower half of the channel at the cross section $x/H = 1.5$. The numerical results are compared with the experimental ones, which were obtained by setting the hole-size parameter equal to $H' = 0$. Ejectionlike motion and sweeplike motion contribute positively to $-\overline{uv}$, while the interactions contribute negatively to $-\overline{uv}$. A negative contribution to $-\overline{uv}$ in the lower half of the channel means that momentum is transferred in the positive y-direction so as to enhance the recovery of the velocity defect in the wake.

At the point α close to the center plane of the channel, Lissajous's figure shows a shape like a letter "X" due to the fact that the frequency of the streamwise velocity fluctuation is twice that of the fundamental frequency or of the normal velocity fluctuation at this position. In this case, the fractional contributions from each quadrant do not differ in magnitude from each other. This results in a small absolute value of correlation $-\overline{uv}$ at this point. On the other hand, at the point β, where $-\overline{uv}$ takes a big negative value, most portions of Lissajous's figure are found in the first and third quadrants, which correspond to the interactive fluid motions. The experimental data shown in Figure 13 agree well with the numerical data, and the interactive motions are found to be major contributors to $-\overline{uv}$. This fact provides another validation of the present numerical procedure. Comparing Figures 9, 10, 11, 12, and 13, the wallward interaction corresponding to the third quadrant is related to the decelerating fluid motion occurring in the front region of the NW tongue, and the outward interaction is related to the accelerating upward motion of the tip of the NW tongue and of the interface between the PS layer and the NW tongue. It is interesting to note that a kinship exists between the present flow and a turbulent boundary layer disturbed by a cylinder (Kawaguchi et al. 1984; Suzuki et al. 1988; Suzuki et al. 1991). First, in both flows, a dissimilarity is found between the momentum transfer and the heat transfer. In the latter flow, it was concluded that the intensification of interactive fluid motion caused the dissimilarity between the momentum transfer and the heat transfer, and therefore the reduction of skin friction. In the present case, the interactive fluid motion also occurs conspicuously. Such fluid motion is effective in enhancing the recovery of the wake behind the rod or in reducing the velocity defect in the wake. However, at the same time, a reduction of the wall skin friction also occurs. As already pointed out, a wall vortex forms near the wall due to the fluid motion induced by the NW tongue. At the locations where this wall vortex appears, instantaneous wall shear stress becomes negative. This leads to the reduction of the time-averaged shear stress indicated by the small but positive value of $-\overline{uv}$ at the point γ, as is shown in Table 1. This reduction is similar to the reduction of skin friction observed in a disturbed turbulent boundary layer (Kawaguchi et al. 1984; Suzuki et al. 1988;

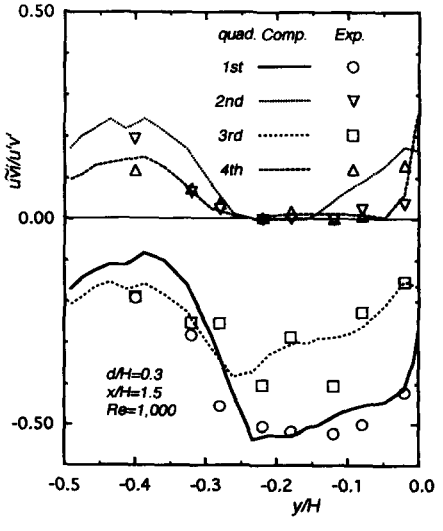

Figure 13 Fractional contributions from the ith quadrant to $\overline{uv}$ when $H' = 0$

Suzuki et al. 1991). Table 1 reveals that the correlation coefficient $\overline{uv}/u'v'$ can be as high as 0.9 at the point β. This value might be reduced noticeably by the three-dimensional (3-D) effect if it appears. Suzuki et al. (1993) found that two-dimensionality was found to be a good approximation of the actual flow, at least in the region $x/H < 3.5$ at the Reynolds number Re = 1,000. However, future study must determine how sensitively this reduction of correlation coefficient due to 3-D flow occurs at higher Reynolds numbers. In this connection, the application of 3-D unsteady numerical computation to the present type of unsteady flow should be interesting.

The normal velocity, V_P, at the center of a vortex shed from the rod is examined next. Figure 14a shows the time variation of the velocity for a vortex having positive vorticity. For comparison, the counterpart of the case where a rod is located in a uniform flow is also plotted. In the latter case, the rod-size Reynolds number was kept at the same value of 150 as the confined-flow case discussed above. Here, the center of the vortex, $P(x_P, y_P)$, was defined as the point where the vorticity takes a local-maximum value. This vortex corresponds to the Karman vortex shed from the lower side of the rod. The variation of the cross-stream position y_P of the vortex is shown for each case in Figure 14b. The labels (a), (c), (e), and (g) inserted in the figures indicate the corresponding frames of Figures 6 through 9 for the confined-flow case, and a prime indicates that the result was obtained in the cycle before $\omega t = 0$. The same method of labeling will also be used in Figure 16.

In both these cases, the local maximum of vorticity cannot be identified in the streamwise region very close to the rod. At the instant when the local maximum of vorticity becomes identifiable at a position of shortest distance from the rod, the normal velocity induced at the center of the vortex takes a positive and high value for both cases. From that instant, the velocity decreases quickly and at one point begins to take a negative value. However, it returns to a positive value within a short time period for the confined-flow case, while it continues to take a negative or almost zero value for the uniform-flow case. For the confined-flow case, after V_P takes its peak value at $\omega t = (1/4)\pi$ (corresponding to Figure 7b), V_P continues to stay positive for a long time—up to $\omega t = 5\pi$. This corresponds to the crisscross motion of the vortex. The vortex crosses the center plane between the instants $\omega t = (1/2)\pi$, corresponding to Figure 7c, and $\omega t = (3/4)\pi$, corresponding to Figure 7d. After $\omega t = 5\pi$, however, the value of V_P decreases to zero, and therefore no return of the vortex to the original side of the channel occurs. On the other hand, the value of V_P in the uniform-flow case takes a negative sign or zero all the way. No crisscross motion is observed in this case.

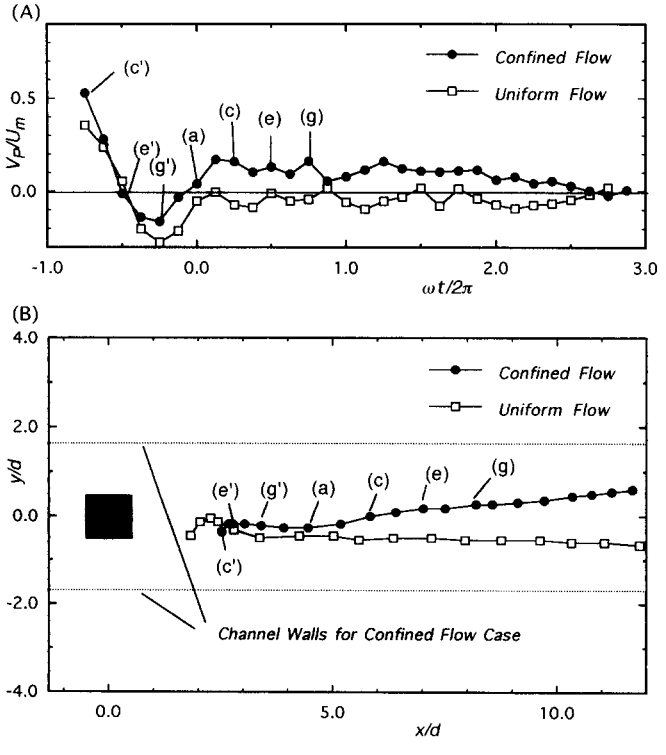

Figure 14 Normal velocity and movement of a Karman vortex. (a) Normal velocity variation of the vortex P; (b) movement of the vortex P

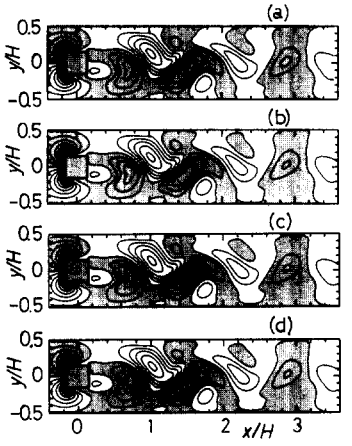

Figure 15 Normal velocity contours for the confined flow case; (a) Obtained by Equation 2 directly; (b) without mirror images; (c) with the first mirror images; (d) with the first and second mirror images

Lastly, in order to deepen the understanding of the crisscross motion of the Karman vortex found by Suzuki et al. (1993), attention is given to the distribution of normal velocity V. Here, V is recalculated from the spatial distribution of the calculated vorticity by making use of Biot–Savart's law. The normal velocity, $V_d(x, y)$, to be induced by the effect of every element of distributed vorticity, $\Omega(\xi, \eta)$, is reproduced for each case by making use of the following equation:

$$V_d(x, y) = \iint_S \frac{1}{2\pi} \frac{\Omega(\xi, \eta) \cos\theta}{\sqrt{(x-\xi)^2 + (y-\eta)^2}} \, d\xi \, d\eta \tag{8}$$

where $\iint_S d\xi d\eta$ is the integration over the entire computational domain and θ is the angle between the y-direction and the velocity vector induced at a point (x, y) by each element of the distributed vorticity. The use of Equation 8 does not ensure zero normal velocity across the solid surface. To see the significance of this effect, three types of approximations were examined for the present case. The first approximation was to use Equation 8 without any modification. The second one took into account the first mirror images of the distributed vorticity elements with respect to each of the channel walls. The third one additionally took into account the second approximation, i.e., the mirror-images of the first mirror-images with respect to other side of the channel walls, in addition to the first mirror-images themselves. Figure 15a shows the contours of the normal velocity V calculated directly from Equation 2. On the other hand, Figures 15b through 15d show the similar contour of V_d reproduced by the three types of approximations mentioned above, respectively. The shaded portions of the

figures correspond to the positive region of V or V_d, and unshaded parts correspond to the negative region of V or V_d in these figures. In a comparison of Figure 15b with Figures 15c and 15d, accounting for the mirror-images incurs very minor modification of V_d distribution. Figure 15b, which presents the contours of V_d calculated by using Equation 8, agrees very well with the actual contours of V obtained directly from Equation 2 and shown in Figure 15a, except for thin layers near the walls. None of the three approximations is at all effective in reducing the magnitude of the nonzero normal fluid velocity across the rod surface. However, no significant difference is observed between the contours of V_d around the rod as plotted in Figures 15b, 15c, or 15d, and the counterparts of V as plotted in Figure 15a. In addition, only a small inaccuracy in the present method is incurred by using Equation 8 without any modification. Therefore, the results of this method will next be used to discuss the behaviors of Karman vortices existing in the central part of the flow space at some distance from the rod.

To discuss which elements of the distributed vorticity make a large enough contribution to such normal velocity to cause the crisscross motion of a Karman vortex in the confined flow case, the value of V_P at a point $P(x_p, y_p)$ as illustrated in Figure 14 was decomposed into the fractional contribution $dV_P(x_P, y_P; \xi, \eta)$ from a vorticity element at a point (ξ, η). It was calculated by the following equation:

$$dV_P(x_P, y_P; \xi, \eta) = \frac{1}{2\pi} \frac{\Omega(\xi, \eta) \cos\theta}{\sqrt{(x_P - \xi)^2 + (y_P - \eta)^2}} d\xi\, d\eta \qquad (9)$$

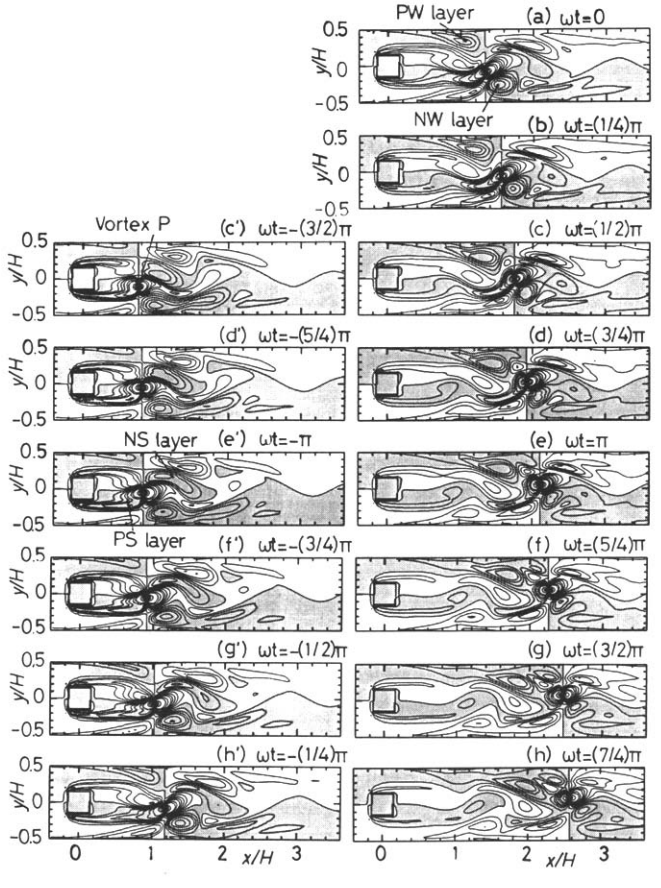

Figure 16 Time variation of the contribution from distributed vorticity to normal velocity induced at the center point of vortex P for the confined flow case

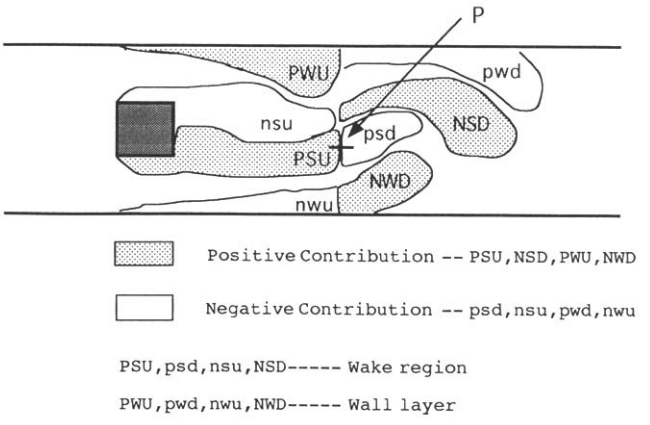

Figure 17 Clarification of the part primarily contributing to V_P

The distributions of the fractional contribution dV_P calculated at the instants marked by circles in Figure 14 are illustrated in the contours of Figures 16c' to 16h. The shaded portions of the figures correspond to the positive region of dV_P, and the unshaded portions correspond to the negative region of dV_P. The total summation of the fractional contributions dV_P from all elements is certainly equal to the induced normal velocity, $V_P(x_P, y_P)$, at the position $P(x_P, y_P)$.

In Figure 16, four regions are identified as the sources that produce a positive value of V_P, i.e., two near-wall regions designated as the PW (Positive-vorticity Wall) layer and NW (Negative-vorticity Wall) layer in Figure 16a and two other regions corresponding to the tip of the NS layer and the main body of the PS layer as shown in Figure 16e'. The latter two regions can be equally effective in driving the vortex in the case where the rod is mounted in a uniform flow. However, there are no counterparts of the former two regions in the uniform flow case, because there is no channel wall there. Therefore, the latter two regions should be responsible for the positive value of V_P in the confined flow case.

This conclusion is confirmed in Figure 18 below, which shows how the magnitude of the fractional contribution to V_P from each part illustrated in Figure 17 varies with time. The PW, NW, NS, and PS layers are all divided into two parts, i.e., a positively contributing part and a negatively contributing part. Therefore, eight parts are included in Figure 18. In this analysis, the contributions from those elements with an absolute value less than a certain threshold were neglected. In the present study, the threshold value was set equal to 0.015 U_m for the confined-flow case of $d/H = 0.3$ and equal to 0.005 U_m for the uniform-flow case. Using these threshold values, each part designated in Figure 17 could be well identified, and the sum of contributions from each part agreed well with the value of V_P for the respective cases. In Figure 18b, in which the results for the uniform flow case are plotted, only the fractional contributions from the four parts corresponding to the wake of the rod appear, and their sum shows zero or negative value except at a very early stage. In contrast to this, in Figure 18a, in which the results of the confined flow case of $d/H = 0.3$ are plotted, the fractional contributions from the other parts located near the channel wall appear, and their sum takes a positive value, as shown in the figure. This positive contribution from these four parts exceeds in magnitude the sum of the fractional contributions from the other four parts and therefore results in the positive value of V_P. Among the former four parts, there are two parts for which the fractional contribution is positive near the wall, i.e., the regions PWU (PW Upstream part) and NWD (NW Downstream part). Therefore, the

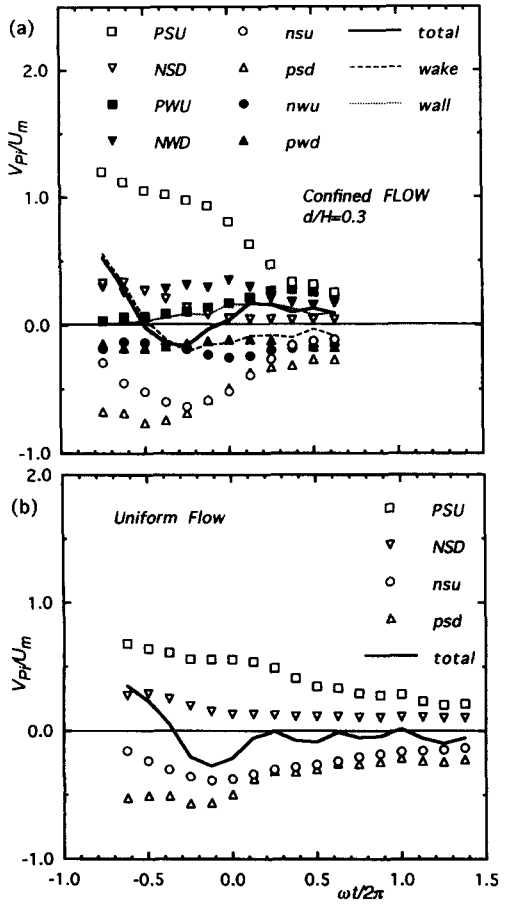

Figure 18 Fractional contribution to V_P from each region. (a) For the case when a rod is located in a channel flow; (b) for the case when a rod is located in a uniform flow

essential mechanism of the crisscross motion of vortices is considered to be as follows: The vortex P under the discussion and the lifted tip of the wall-vorticity layer NWD are counterrotating each other. As is well established, counterrotating vortices having the same magnitude of circulation create translational motion, since translational motion somehow occurs for the pair composed of the vortex P and the tip of the wall layer NWD. The translational motion under discussion moves along the direction perpendicular to the line passing through the centers of those vortices. Thus, it has a positive velocity-component value for V_P. This motion is reinforced by the action exerted by another wall layer, PWU. The wall layer PWU is corotating with the vortex P and exerts anticlockwise circular motion at the center of the vortex P. The motion, however, is less noticeable than the one discussed above.

Concluding remarks

A numerical study was carried out for a periodically changing unsteady flow in a channel obstructed by an inserted rod. The studied flow is highly periodic, and is therefore almost free from randomness or irregularity. Consequently, it is quite different from turbulent flows. However, the obtained results reveal that the momentum transfer is enhanced due to the apparent shear stress resulting from the nonzero value of cross-correlation between the streamwise and normal components of the fluctuating velocity. Rapid recovery of velocity field proceeds at some positions in the wake of the rod due to the nonzero value of $\overline{uv}$. The nonzero value of $\overline{uv}$ was confirmed by the experimental data measured with hot-wire anemometry. Based on the computational results, the time variation of the instantaneous flow structure of the flow was also discussed. The separation layer that develops on either side of the rod, in which vorticity is high in magnitude, shows wavering motion with the passage of time, as well as elongation and thinning at its neck. Thus, its tip is periodically disconnected from the main part of the separation layer. The shedding of the Karman vortex occurs as a result of this disconnection. After the tip is disconnected, it divides into two parts. Its main part crosses the center plane of the channel. Another important structure of the flow is that of the near-wall region. The high-vorticity wall layer, strengthened in vorticity due to flow acceleration at the side of the rod, is exposed to a strong adverse pressure gradient in the region downstream of the rod, and its separation from the wall occurs. The tip of this lifted tongue of the wall layer is also periodically disconnected and forms an isolated vortex island. The interference between this isolated vortex island and the downstream tip of the separation layer causes the crisscross motion of the Karman vortex. The mechanism for the generation of a nonzero value of $\overline{uv}$ is also related to the interference. Wallward and outward interactive fluid motions occur, respectively, at the front and back sides of the isolated vortex island or the disconnected tip of the high-vorticity wall layer, and they produce nonzero value of $\overline{uv}$. They are also related to the negative value of instantaneous wall shear stress occurring within the wall vortex, which is formed by the flow induced around the isolated vortex island. The motion of a Karman vortex is affected by the distribution pattern of vorticity in the flow space. In particular, mutual interference between the vortex shed from the rod and the downstream tip of the high vorticity wall layer is important. When d/H is not small enough, the downstream tip of the wall layer is lifted up from the channel wall by the effect of the vortex shed from the rod. The lifted tip of the wall vorticity layer reciprocally assists the vortex shed from the rod to cross the center plane. This mutually assisting interference is the mechanism of the crisscross motion of the Karman vortex. Therefore, the generation of the lifted tongue of the wall vorticity layer thick enough in size and high enough in vorticity is vital for the generation of the crisscross motion of Karman vortex.

Acknowledgment

The authors gratefully acknowledge the partial support of this study given through the Grant in Aid of Scientific Research of the Ministry of Education, Science and Culture, Japan, No. 01603523.

References

Davis, R. W. and Moore, E. F. 1982. A numerical study of vortex shedding from rectangles. *J. Fluid Mech.*, **116**, 475–506

Davis, R. W., Moore, E. F., and Purtell, L. P. 1984. A numerical–experimental study of confined flow around rectangular cylinders. *Phys. Fluids*, **27**(1), 46–59

Deng, G. B., Piquet, J., Queutey, P., and Visonneau, M. 1993. Flow past a square cylinder predictions with an eddy-viscosity model. *Proc. 9th Symp. Turbulent Shear Flows* (10.2.1–10.2.6), Kyoto

Frank, R. and Rodi, W. 1991. Calculation of vortex shedding past a square cylinder with various turbulence models. *Proc. 8th Symp. Turbulent Shear Flows* (20.1.1–20.1.6), Munich

Karniadakis, G. E., Mikic, B. B., and Patera, A. T. 1988. Minimum-dissipation transport enhancement by flow destabilization: Reynolds' analogy revisited. *J. Fluid Mech.*, **192**, 365–391

Kato, M. and Launder, B. E. 1993. The modeling of turbulent flow around stationary and vibrating square rod. *Proc. 9th Symp. Turbulent Shear Flows* (10.4.1–10.4.6), Kyoto

Kawaguchi, Y., Matsumori, Y., and Suzuki, K. 1984. Structural study of momentum and heat transport in the near wall region of a disturbed turbulent boundary layer. *Proc. 9th Biennial Symp. Turbulence* (28.1–28.10), Rolla, Missouri

Kawall, J. G., Shokr, M., and Keffer, J. F. 1983. A digital technique for the simultaneous measurement of streamwise and lateral velocities in turbulent flows. *J. Fluid Mech.*, **133**, 83–112

Kikuchi, Y., Ohno, Y., and Takahashi, M. 1993. The effect of pulsating flow on combined forced and free convective heat transfer from a cylinder in crossflow. *Proc. 1st Int. Thermal Energy Congress*, **1**, 217–220

Lehmann, G. L. and Wirtz, R. A. 1988. Effect of variations in streamwise spacing and length on convection from surface-mounted rectangular components. *Heat Transfer Eng.*, **9**(3), 66–75

Leonard, B. P. 1979. A stable and accurate convective modeling procedure based on quadratic interpolation. *Comput. Meth. Appl. Mech. Eng.*, **19**, 59–98

Lu, S. S. and Willmarth, W. W. 1973. Measurements of the structure of the Reynolds stress in a turbulent boundary layer. *J. Fluid Mech.*, **60**(3), 481–511

Majumdar, D. and Amon, C. H. 1992. Heat and momentum transport in self-sustained oscillatory viscous flows. *J. Heat Transfer*, **114**, 866–873

Nagano, Y. and Tagawa, M. 1988. An error analysis of hot-wire measurements. *Trans. JSME*, **54**(503), 1642–1648 (in Japanese)

Nishihara, A., Suzuki, K., and Inoue, Y. 1988. Numerical computation of flow and heat transfer in a channel with a sudden expansion. *Proc. Natl. Heat Transfer Symposium of Japan*, **2**, 76–78 (in Japanese)

Patankar, S. V. and Spalding, D. B. 1972. A calculation procedure for heat, mass and momentum transfer in three-dimensional parabolic flows. *Int. J. Heat Mass Transfer*, **15**, 1787–1806

Perry, A. E. 1982. *Hot-wire Anemometry*. Clarendon Press, Oxford

Suzuki, H. 1990. Study on heat transfer under an unsteady flow obstructed by a cylindrical body. Doctor thesis, Dept. of Mechanical Engineering, Kyoto University, Kyoto, Japan (in Japanese)

Suzuki, H., Inoue, Y., Nishimura, T., Fukutani, K., and Suzuki, K. 1993. Unsteady flow in a channel obstructed by a square rod (crisscross motion of vortex). *Int. J. Heat Fluid Flow*, **14**(1), 2–9

Suzuki, H., Suzuki, K., and Sato, T. 1988. Dissimilarity between heat and momentum transfer in a turbulent boundary layer disturbed by a cylinder. *Int. J. Heat Mass Transfer*, **31**(2), 259–265

Suzuki, K. and Suzuki, H. 1994. Unsteady flow heat transfer in a channel obstructed with an immersed body. *Annu. Rev. Heat Transfer*, Vol. 5, C. L. Tien (ed.). Begell House, New York, 177–206

Suzuki, K., Kieda, S., Chichiki, T., and Sato, T. 1981. Numerical study of combined convective heat transfer with variable fluid properties in the inlet region of a circular tube. In *Numerical Methods in Laminar and Turbulent Flow*, R. W. Lewis et al. Pineridge Press, Swansea, UK, 1048–1059

Suzuki, K., Suzuki, H. Kikkawa, Y., Kigawa, H., and Kawaguchi, Y. 1991. Study on a turbulent boundary layer disturbed by a cylinder—effect of cylinder size and position. In *Turbulent Shear Flows*, vol. 7, F. Durst (ed.). Springer-Verlag, Berlin, 119–135

Tatsutani, K., Devarakonda, R., and Humphrey, J. A. C. 1993. Unsteady flow and heat transfer for cylinder pairs in a channel. *Int. J. Heat Mass Transfer*, **36**(13), 3311–3328

Xi, G. N., Suzuki, K., Hagiwara, Y., and Murata, T. 1989. A basic study on heat transfer characteristics of offset fin arrays—Effect of fin thickness in the middle range of Reynolds number. *Trans. JSME Ser. B*, **55**(519), 3507–3514 (in Japanese)